Modes and break periods of electrowetting liquid bridge

Mohsen Torabi,[1,*] Ahmed A. Hemeda,[1,2,*] James W. Palko,[1] Yu Feng,[3] Yong Cao,[3] and Yanbao Ma[1,†]
[1]*School of Engineering, University of California, Merced, California 95343, USA*
[2]*Aerospace Engineering Department, Cairo University, 12613 Egypt*
[3]*Harbin Institute of Technology, Shenzhen, Guangdong 518055, People's Republic of China*

(Received 10 May 2019; revised manuscript received 21 July 2019; published 11 September 2019)

In this paper, we propose a microscale liquid oscillator using electrowetting-on-dielectric (EWOD). Specifically, a mesoscale liquid bridge (LB) between two horizontal surfaces with EWOD is considered. When EWOD is applied, the solid surface becomes more hydrophilic, and hence the contact angle (CA) is reduced. Following the activation of EWOD, the LB can remain connected or it can break into either symmetric or asymmetric shapes depending on the initial liquid volume and wettability of the two surfaces. The LB dynamics activated by EWOD is studied using the multibody dissipative particle dynamics (MDPD) method. Our numerical results show that the behavior of an LB under EWOD can be interpreted via three modes. In the first mode, the LB does not break after applying EWOD. In the second mode, the LB breaks and does not reform. The third mode happens when, depending on the interplay of the volume of the liquid and CA manipulation, the LB continuously breaks, recoils, and reforms. For asymmetric cases, it was observed that the LB may completely detach from one surface and may not reform. It was also observed that decreasing the wettability of a surface, for cases with a continuous breaking and reformation behavior, increases the connecting time interval and decreases the breaking time interval in one break-reform cycle. The results provided in this investigation facilitate fundamental understanding of LB dynamics and their application for the design of microscale liquid oscillators using EWOD.

DOI: 10.1103/PhysRevE.100.033102

I. INTRODUCTION

Microfluidics combines both the science and the technology of manipulating and controlling fluids in small scales, usually in the range of microliters to picoliters [1]. Digital microfluidics is an attractive branch of microfluidics, providing a platform for lab-on-a-chip systems [2,3]. By using various techniques to modify different characteristics of fluids and surfaces such as wettability, droplets are successfully moved, mixed, separated, or stored on a platform with a set of microscale devices [2–4]. The tendency for wetting of a surface can be modified by various approaches such as introducing roughness [5] or changing chemical properties of the surface [6–8]. The surface morphology and chemical properties provide certain boundary conditions which guide the liquid to the most energetically minimized position, and hence shape the desired configuration [9,10]. A downside of chemical and topographical patterns is their fixed nature, which means that these patterns cannot be modified after construction [11].

The wettability of a surface can also be modified by artificially increasing the energy of a surface using an electrostatic force between the surface and liquid [12,13]. Unlike chemical and topographical patterns, electrostatic forces provide a great degree of switchability and long-term durability [14,15]. This technique, commonly called electrowetting (EW), was introduced by Lippmann in 1875 [11]. To limit current and prevent electrolysis in the liquid at high actuation voltages, the conductive liquid and the metallic electrode should be separated. This has been addressed via electrowetting-on-dielectric (EWOD) by Berge [16]. By using EWOD, the droplet is controlled by the applied voltage at the electrode just below the substrate surface. By applying the voltage, a charge at the liquid-solid interface is created and the interfacial energy is locally reduced. This generates a flow in the direction of low interfacial energy, and consequently, the contact angle (CA) of the liquid is modified to a reduced value. To fully utilize the potential of EWOD and to deal with more complex situations, various improvements and developments such as optoelectrowetting have been sought [17].

Given EWOD's precise controllability, accurate modification of values of CA for a liquid droplet on a surface can be accomplished. It has been shown that by applying different voltages, different CAs, reduced to less than 20°, can be achieved [18,19]. Although EWOD is still a new technique, there have been extensive investigations on this topic due to its potential for both scientific and industrial applications. By way of fundamental investigations, firstly, various experiments on the relation between CAs and applied voltages have been carried out [18,19]. EW-induced droplet spreading and detachment in conventional ambient [20–22] and oil environments [23] for stationary configurations have been investigated. The effect of voltage magnitude on the advancing and receding CAs was also studied [24]. Controlling the CA of liquid drops on different surfaces via EWOD was proven to be effective to control the permeability of porous structures [25] and to assist bubble detachment from a liquid film [26]. It was also shown that by controlling the applied

*These authors contributed equally to this work.
†yma5@ucmerced.edu

voltage between two surfaces of a wedge, the position and shape of liquid drops confined in the wedge can be precisely controlled [27]. An interesting recent experiment also showed that by choosing specific parameters in a precisely designed configuration, the angle of ballistic ejection of liquid drops can be accurately manipulated via electrostatic forces [28].

EWOD has also found numerous practical applications from smart optics [29] to energy harvesting [30] and liquid resonators [31]. Shortly after the introduction of EWOD in 1993 [16], it was employed in cameras to change the focal length of lenses [32]. By taking advantage of manipulating the air-water interface via EW, a centimeter-sized boat without complicated propulsion mechanisms was invented [33]. Because of the precisely controllable nature of EW, reconfigurable optofluidic slits without mechanically moving parts have also been realized [34]. EW has shown extensive applicability in three-dimensional digital microfluidics such as accurate manipulation and mixing of different droplets with various chemical properties [35]. While the above-mentioned applications have used EW in an actuation manner, a similar application showed the capability of this phenomenon for harvesting energy in small scale geometries [30,36].

As mentioned before, by applying EWOD via a voltage difference between upper and lower surfaces, the solid surfaces become more lyophilic via an electrostatic force applied on the liquid-solid interfaces. This dynamic force consequently reduces the CA of the droplet and causes the droplet to deform. By removing the applied voltage on the system, the liquid would recoil and tend to recover its original configuration. If the potential energy within the liquid droplet corresponding to the surface tension is sufficient, the droplet may detach from the surface [22,28]. On the other hand, if the process is happening in a confined environment the droplet may jump from one surface to another, which has been recently demonstrated [35]. Another potential configuration is a capillary bridge between two surfaces [27,11,37]. If a liquid bridge (LB) forms between two parallel EW surfaces, the meniscus of the bridge can be modified by applying a voltage between the upper and lower walls, and the LB may break [38]. After bridge breaking, the applied voltage appears mainly across the gap, reducing the electric field at the liquid-solid interfaces, and the liquids on each surface would recoil. Depending on the maximum recoiling and jumping height, the two liquid parts may touch each other, and the bridge formation and disruption may continue.

Although there has been an experimental investigation on the behavior of an LB under electrostatic forces [38], there is no comprehensive analysis of this phenomenon. An LB under electrostatic forces may change its shape and form a neck somewhere between the upper and lower surfaces. Depending on the original wettability of the upper and lower surfaces, the LB can be symmetric or asymmetric. Hence, by introducing EW, an LB may form a symmetric or asymmetric neck and may break.

The present investigation deals with a mesoscale LB-EWOD system to shed light upon the different break mechanisms and modes of the LB, and to provide fundamental understanding on different stages of this phenomenon. To model a mesoscale LB, the multi-body dissipative particle dynamics (MDPD) method is used. Simulation details and features of MDPD are elaborated in Sec. II. Then, the investigated configuration and its geometrical specifications are given in Sec. III. Section IV provides an in-depth illustration and discussion on the various modes and styles of the breakup or reconfiguration of the bridge. Finally, Sec. V gives conclusions and remarks regarding the implications of these processes for the application of EWOD.

II. MDPD SIMULATION

A. Governing equations

MDPD is an extension to the mesh-free, coarse-grained molecular dynamics (MD) dissipative particle dynamics (DPD) simulation approach [39]. Unlike DPD, MDPD is capable of simulating unconfined geometries. In this method, a cluster of several molecules forms each particle. This method also includes Brownian motions within the simulation, which are crucial at these small scales. The length and timescales in MDPD are between atomistic and continuum approaches [40,41], which is an advantage of this method. Ghoufi and Malfreyt [42] have shown that the computational cost of MDPD is 20 times lower than MD simulation to achieve the same real time.

To model the motion of each MDPD particle or "bead," Newton's second law is used as follows:

$$\frac{d\vec{r}_i}{dt} = \vec{v}_i, \tag{1}$$

$$m_i \frac{d\vec{v}_i}{dt} = \vec{f}_i = \sum_{j \neq i} \left(\vec{f}_{ij}^{C} + \vec{f}_{ij}^{D} + \vec{f}_{ij}^{R}\right) + \vec{g}, \tag{2}$$

where $\vec{r}_i$, $\vec{v}_i$ and $\vec{f}_i$ denote the ith bead's position, velocity, and total force, respectively. The external body force exerted on each particle is incorporated into the model by parameter $\vec{g}$, which can be neglected here because of the particle size and operating condition [43,40,44]. The conservative force $\vec{f}_{ij}^{C}$, dissipative force $\vec{f}_{ij}^{D}$ and random force $\vec{f}_{ij}^{R}$ are given by [41,45]

$$\vec{f}_{ij}^{C} = A_{ij}\omega_c(r_{ij}, R_c)\vec{e}_{ij} + B_{ij}(\bar{\rho}_i + \bar{\rho}_j)\omega_c(r_{ij}, R_d)\vec{e}_{ij}, \tag{3}$$

$$\vec{f}_{ij}^{D} = -\gamma\omega_D(r_{ij}, R_c)\left(\vec{e}_{ij} \cdot \vec{v}_{ij}\right)\vec{e}_{ij}, \tag{4}$$

$$\vec{f}_{ij}^{R} = \varphi\omega_R(r_{ij}, R_c)\theta_{ij}\Delta t^{-1/2}\vec{e}_{ij}, \tag{5}$$

where the subscript j stands for neighbor particles to the particle i [i.e., $j \in S_i$, see for instance Fig. 1(c)]. Also, $r_{ij} = |\vec{r}_{ij}|$, $\vec{r}_{ij} = \vec{r}_i - \vec{r}_j$, $\vec{e}_{ij} = \vec{r}_{ij}/|\vec{r}_{ij}|$, and $\vec{v}_{ij} = \vec{v}_i - \vec{v}_j$. A_{ij} and B are the attractive and repulsion force amplitudes with weighting functions of ω_C with two different cutoff radii R_c and $R_d = 0.75R_c$, where $\omega_C(r_{ij}, R_c) = \max(1 - r_{ij}/R_c, 0)$. γ and φ are the dissipative and random force amplitudes. Stability conditions require that $\omega_R = \sqrt{\omega_D}$ and $\varphi^2 = 2\gamma k_B T$, where k_B is Boltzmann constant and T is the temperature of the system. The parameter θ_{ij} is sampled from a Gaussian white noise distribution with unit bandwidth, and Δt is the time step. Warren proposed an empirical density-dependent conservative force formula with cut-off range R_d. The local

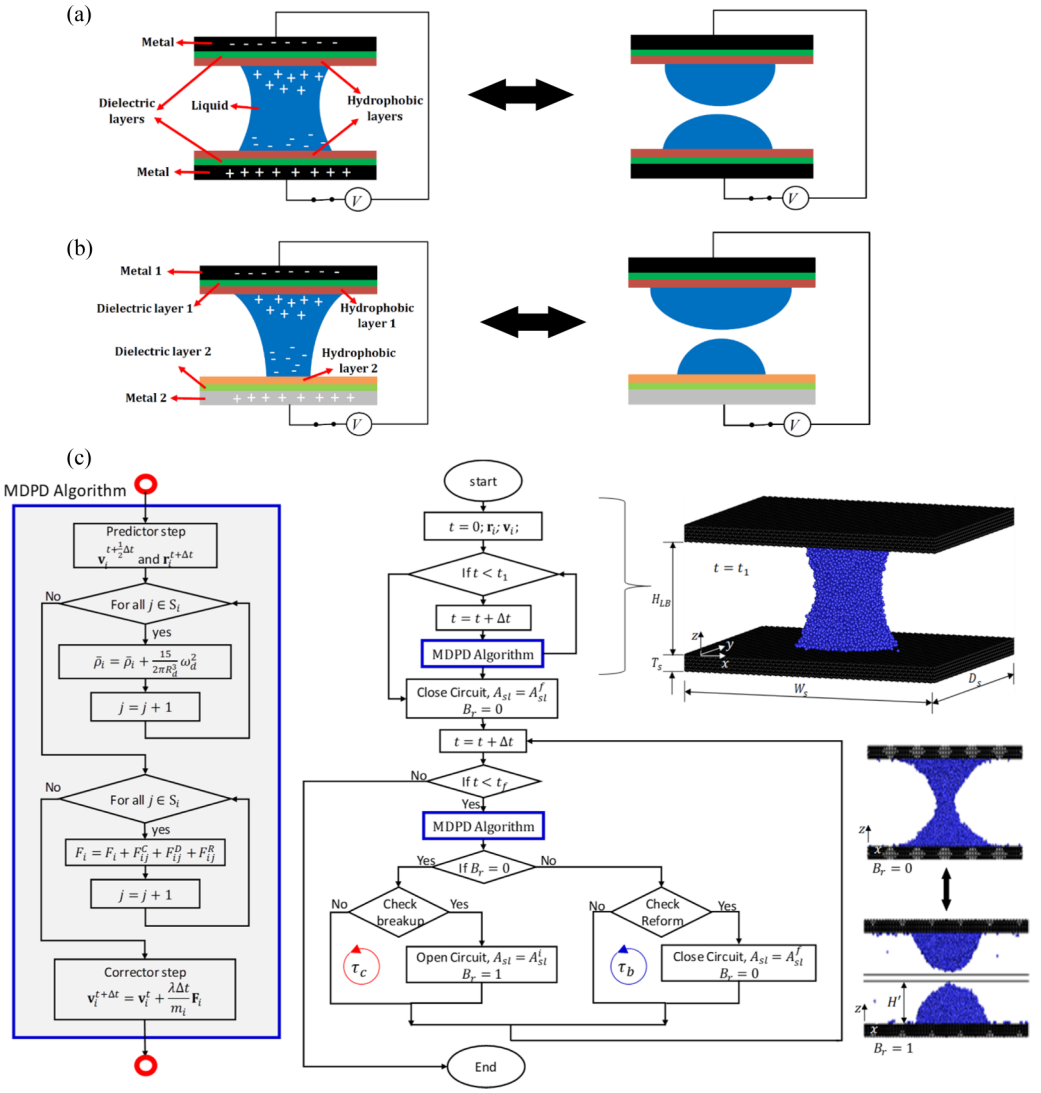

FIG. 1. Schematic of the liquid bridge and its disruption due to electrowettability phenomenon. (a) Symmetric and (b) asymmetric induced electrowetting. (c) The solution algorithm of MDPD, and the present LB-EWOD models. The LB-EWOD examples in (c) include the configuration and dimensional parameters of the present MDPD simulation, and two cases when $B_r = 0$ and $B_r = 1$.

density-function is given by [46]

$$\bar{\rho}_i = \frac{15}{2\pi R_d^3} \sum_{j \neq i} (1 - r_{ij}/R_d)^2. \tag{6}$$

More explanations of forces and parametric values of MDPD can be found in, e.g., Ref. [47].

B. Fluid-structure interaction

In our MDPD implementation, the substrate particles are assumed to be frozen for simplicity [48,49], but their interaction with the fluid is considered. As shown above, forces between beads are soft and short-range interactions [50]. This allows large time steps for the interaction of particles within the system. However, unlike the hard potentials in MD, the soft interaction between beads would not prevent fluid beads from penetrating into walls [51]. To prevent penetration of the fluid beads into the solid part of the system and to ensure the no-slip boundary condition, the bounce-back treatment has been implemented in this work. A simple mathematical manipulation for bounce-back boundary condition for a flat horizontal wall can be written as follows:

$$\overrightarrow{v}_{i,m} = -\overrightarrow{v}_{i,p}, \tag{7}$$

$$\overrightarrow{r}_{i,m} = 2\tau_m(\overrightarrow{r}_{i,o} - \overrightarrow{r}_{i,p}) + \overrightarrow{r}_{i,p}, \tag{8}$$

where

$$\tau_m = (z_w - z_p)/(z_o - z_p). \tag{9}$$

In the above equations the subscripts m, o, p, and w denote modified, old, predicted, and solid wall, respectively. Also, the parameter z is the vertical component of $\vec{r}_i$ which is used to calculate the parameter τ_m that is in the range of 0 and 1.0 [51]. Note that the above-mentioned equations [Eqs. (8) and (9)] are the parametric form of a straight line in 3D.

TABLE I. Parametric values used in MDPD simulation.

Parameter	Symbol	DPD values	Physical values for water/glycerol mixture [52]
Particle mass	m	1.0	5.43×10^{-16} kg
System energy	k_BT	1.0	–
Cut-off radius of attractive force	R_c	1.0	–
Cut-off radius of repulsive force	R_d	0.75	–
Attraction parameter (liquid-liquid)	$A_{\ell\ell}$	−40	–
Repulsion parameters	$B_{\ell\ell}, B_{s\ell}$	25	–
Amplitude of random force	φ	6.0	–
Time step	Δt	0.01	2.49×10^{-9} s
Fluid bead density	ρ	6.10	1137 kg m^{-3}
Liquid-vapor surface tension	σ	7.30	0.064 N m^{-1}
Liquid kinematic viscosity	υ	7.45/6.1	10^{-5} m^{2}s^{-1}

To change the interaction of the fluid with solid walls for different static or dynamic behaviors, only one interaction parameter is modified. This parameter is usually the attraction force amplitude in the conservative force, i.e., A_{ij}, between fluid and solid beads, $A_{s\ell}$ [47]. Hence, the rest of the interaction parameters for the solid/fluid particles remain constant. The parametric values used in this investigation and their representative values in the physical domain have been tabulated in Table I.

C. Dimensional analysis

The MDPD parameters used in the present investigation are provided in Table I. Properties of the working fluid are expressed in the dimensionless form with the transformation to physical units given below. Assuming the fluid density, kinematic viscosity, and surface tension in SI units are d^*, υ^*, and σ^*, respectively, the conversion length L_{DPD}, mass M_{DPD}, and time T_{DPD} are obtained using the following formulas:

$$L_{\mathrm{DPD}} = \frac{d^*}{d}\left(\frac{\upsilon^*}{\upsilon}\right)^2 \frac{\sigma}{\sigma^*}, \tag{10}$$

$$T_{\mathrm{DPD}} = L_{\mathrm{DPD}}^2 \frac{\upsilon}{\upsilon^*}, \tag{11}$$

$$M_{\mathrm{DPD}} = \frac{d^*}{d} L_{\mathrm{DPD}}^3. \tag{12}$$

In Table I, the last three rows (d, σ, and υ) are devoted to the values of fluid density, kinematic viscosity, and surface tension in DPD and physical units. For example, by considering a water/glycerol mixture with wt % of 59 as the working fluid [52], the DPD unit length can be then calculated as

$$L_{\mathrm{DPD}} = \frac{1139\,[\mathrm{kg\,m^{-3}}]}{6.1\,[\mathrm{DPD\ unit}]}\left(\frac{10^{-5}\,\mathrm{m^2\,s^{-1}}}{7.45/6.1\,[\mathrm{DPD\ unit}]}\right)^2 \times \frac{7.3\,[\mathrm{DPD\ unit}]}{0.064\,\mathrm{N\,m^{-1}}}, \tag{13}$$

which results in a physical length of $L_{\mathrm{DPD}} \approx 1.43$ μm for the unit length in nondimensional "DPD units." By following the same notion, the unit time and mass are calculated as $T_{\mathrm{DPD}} \approx 2.49 \times 10^{-7}$ s and $M_{\mathrm{DPD}} = 5.43 \times 10^{-16}$ kg. These values are much larger than the unit values in MD simulations [53]. It should be mentioned that by decreasing the viscosity, density, and surface tension of the fluid in the above equations, the unit length of each DPD can be decreased to the order of nanometers.

III. CONFIGURATION AND SOLUTION ALGORITHM

An LB between two horizontal plates is considered in this investigation. In EWOD experiments, the inner surfaces of metallic plates are covered by a thin layer of dielectric materials, e.g., SU-8, to avoid electrolysis, followed by a hydrophobic layer, e.g., Polytetrafluoroethylene [54,55]. The upper and lower plates are then connected via an applied voltage. Depending on the wetting properties of the upper and lower surfaces, the initial configuration of the bridge can be either symmetric or asymmetric. Schematic of two LB-EWOD systems are shown in Fig. 1. By closing the electric circuit, the LB in Fig. 1(a) deforms symmetrically, and the LB in Fig. 1(b) deforms asymmetrically. For sufficient applied voltage, the LBs may break in a symmetric or asymmetric fashion corresponding to the form of the original bridge. Once the bridge breaks, the applied voltage is mainly manifest across the gap due to the very low dielectric constant of air or vapor filling the gap compared to the liquid. This results in a reduction in the effect of electric field on wettability at the liquid-solid interface. This investigation models similar configurations and phenomena by applying switchable wettability criteria on the upper and lower surfaces by changing $A_{s\ell}$ in the MDPD simulation. Figure 1(c) shows the solution algorithm for modelling the LB between two surfaces under investigation. The details of this algorithm will be given later in Sec. IVB. The LB's height, i.e., the gap between the two parallel surfaces, is $H_{\mathrm{LB}} = 15$ DPD length (or $H_{\mathrm{LB}} = 21.5$ μm), and the three $W_s \times D_s \times T_s$ dimensions of the upper and lower plates in MDPD simulations are kept constant at $40 \times 40 \times 3$, respectively, for all of the case studies. These dimensions are shown in Fig. 1(c). Three different numbers of MDPD beads for the liquid phase, i.e., liquid volumes V, are

TABLE II. Number of liquid and solid particles in each case.

Case Number	Liquid beads/volume, V	Solid beads/volume, V
Case 1	5,508/2,684 μm^3	42,320/20,625 μm^3
Case 2	9,792/4,772 μm^3	
Case 3	13,328/6,522 μm^3	

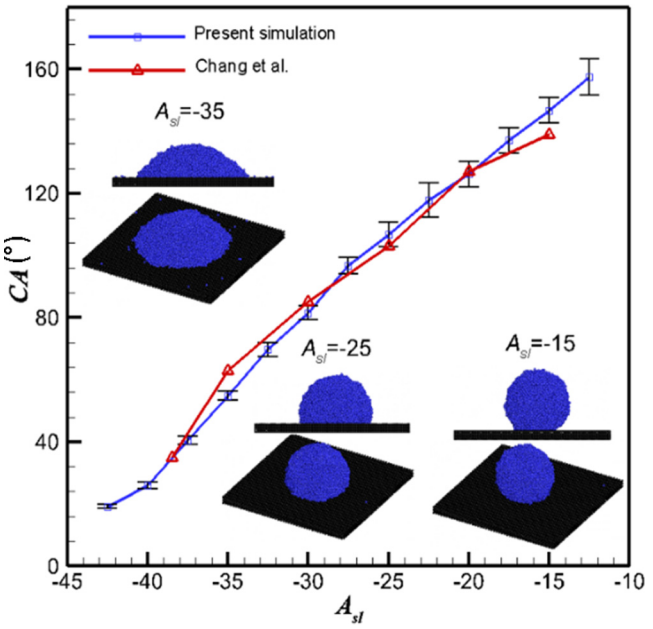

FIG. 2. Comparison of the contact angle of a droplet on a wall using the present MDPD method and provided data by Chang *et al.* [56].

considered for each scenario. The number of liquid and solid beads in each case are given in Table II.

IV. RESULTS

A. Validation

For validation purposes, the effect of $A_{s\ell}$ on the CA of a static droplet on a horizontal flat wall is reported. Figure 2 provides an illustration of this effect. The inset figures show liquid droplets on lyophilic or lyophobic surfaces. Figure 2 shows excellent agreement between the present results for the contact angle of a droplet and the reported MDPD study by Chang *et al.* [56]. As a reference for wettability characteristics of the surfaces considered in the following analyses, the corresponding CA for each $A_{s\ell}$ has been also provided in Table III.

B. Symmetric LB

In this section, a comprehensive analysis of symmetric LB-EWOD is provided. As mentioned before, three different volumes for the liquid phase are considered for each parametric study, which are given in Table II. After assigning an initial

TABLE III. CA versus $A_{s\ell}$ for a liquid droplet on a solid surface using the MDPD method.

$A_{s\ell}$	CA	$A_{s\ell}$	CA
−10	167 ± 5.7	−30	81 ± 2.2
−15	147 ± 4.1	−35	55 ± 1.5
−20	126 ± 4.0	−40	26 ± 1.0
−25	107 ± 3.8		

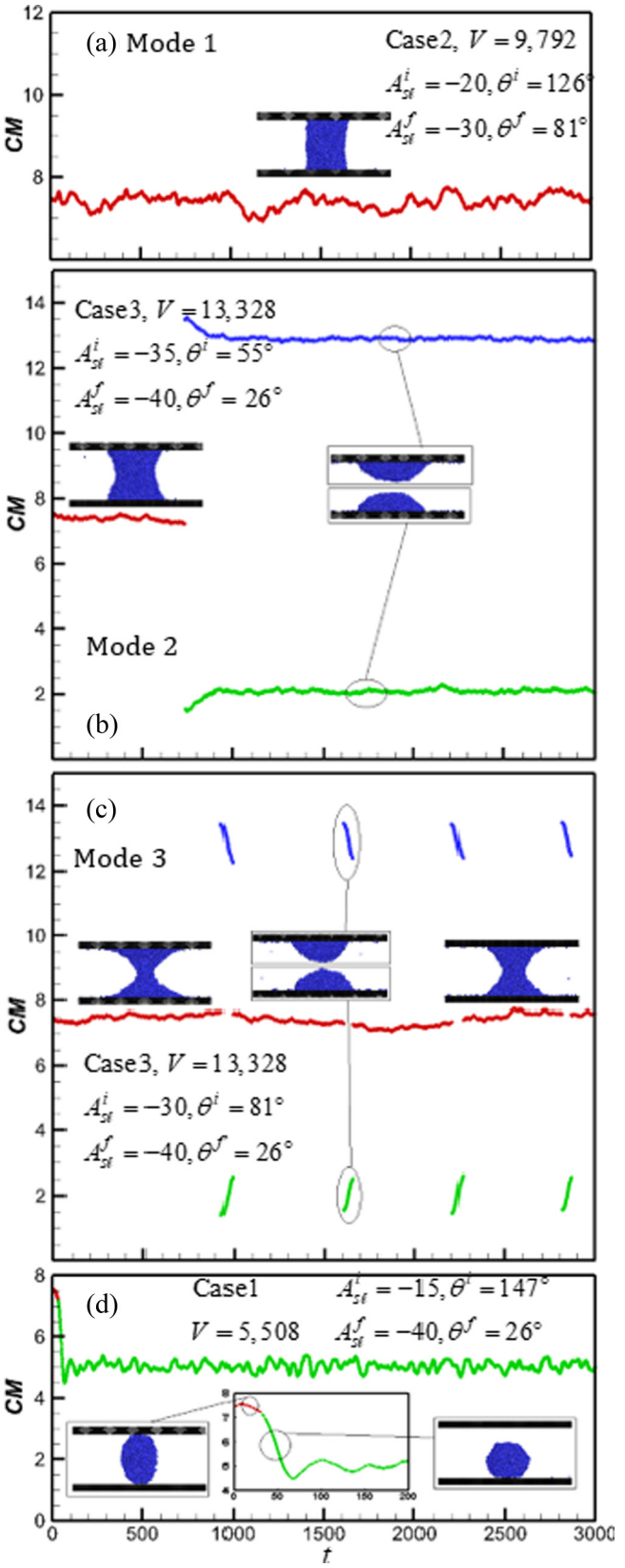

FIG. 3. Center of mass (CM) for different models of the electrowetting bridge. (a–c) Modes 1 to 3, respectively. (d) Example unstable liquid bridge for high original CA. The CM position shown as red, blue, and green curves are for the complete bridge and the upper and lower portions of the droplet, respectively.

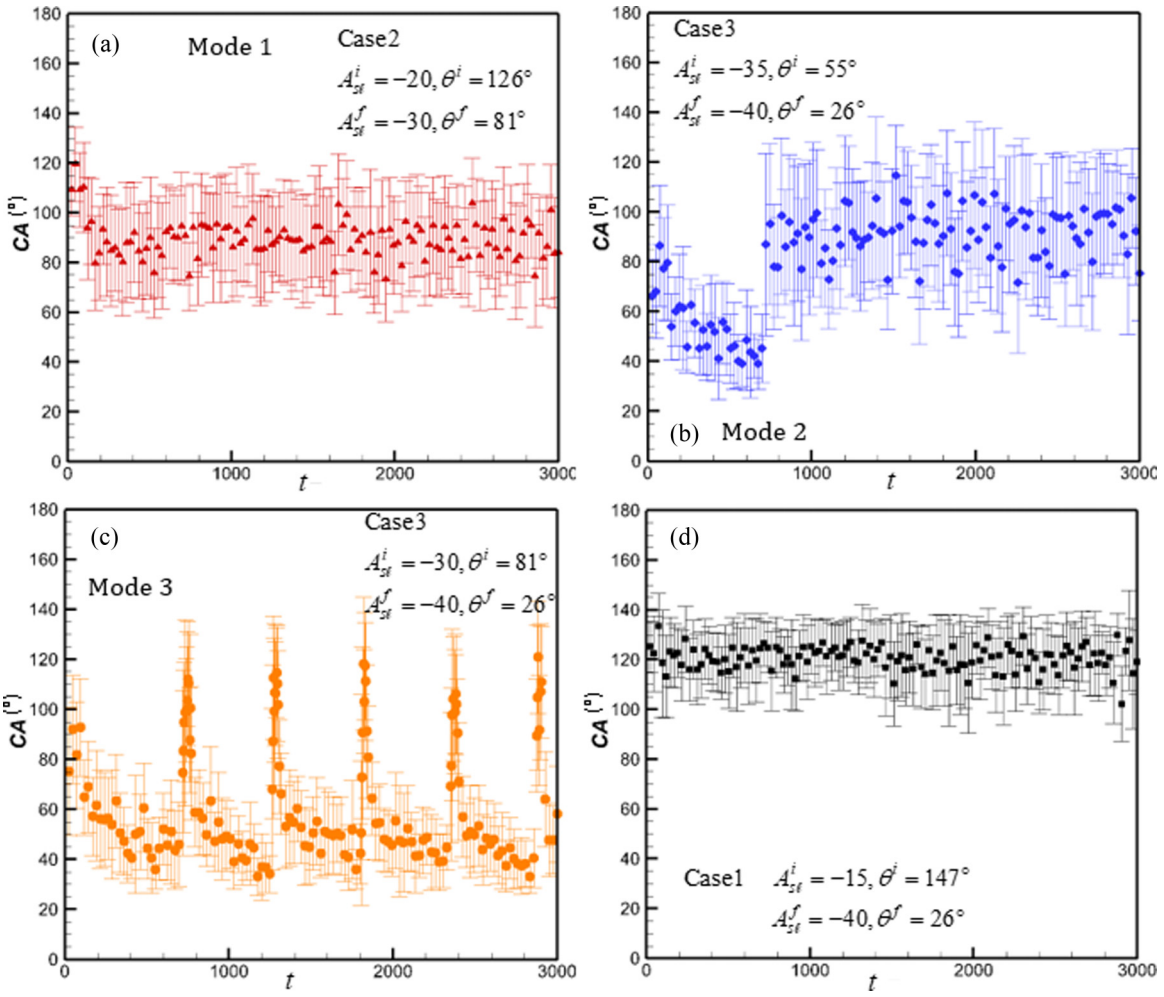

FIG. 4. Dynamic contact angles for different models of the electro-wetting bridge. (a–c) Modes 1 to 3, respectively. (d) Example unstable liquid bridge for certain original CAs.

$A_{s\ell}$ value on each surface, a final $A_{s\ell}$ value is assigned to each surface to modify the LB meniscus and possibly break the bridge. Hereafter, the superscript i and f for $A_{s\ell}$ represents the initial and final $A_{s\ell}$ values, respectively. Figure 3, which represents the analysis of the symmetric EWOD system in Fig. 1(a), shows examples for different modes of LB and its response to a sudden change of $A_{s\ell}$ value on both surfaces. These modes result from the interplay of $A_{s\ell}^i$, $A_{s\ell}^f$, and LB volume, as will be discussed later. From $t = 0$ to $t = t_1 = 100$ DPD time units the values for wettability of the upper and lower surfaces are kept at $A_{s\ell}^i$. t_1 should be large enough to ensure convergence to a steady state. Then, the dynamic process begins at $t = t_1 = 100$ by switching the $A_{s\ell}^i$ to $A_{s\ell}^f$. A new variable, B_r, is defined for the LB breakup or reformation. $B_r = 0$ means that the LB is intact, whereas $B_r = 1$ indicates breaking of the bridge. To determine B_r, we divide the space between the parallel plates into $N = 15$ vertical bins ($H_{\mathrm{LB}} = 15$ DPD), then the average local density is calculated within each bin. If this average local density approaches zero in any of these bins, then the LB is considered broken, i.e.,$B_r = 1$. This approach was adopted from local density calculations in molecular dynamics [57,58]. If the LB breaks, then the electric field is dramatically reduced at the liquid-solid interface, and $A_{s\ell}^f$ changes back to $A_{s\ell}^i$, causing the liquid to recoil [see, for instance, Fig. 1(c)]. The periods, τ_c (when $B_r = 0$) and τ_b (when $B_r = 1$), are calculated within each loop with the same value B_r. This will be discussed later.

Generally speaking, there are three modes for the behavior of a symmetric LB under the influence of EWOD. These three modes are shown in Figs. 3(a)–3(c) based on the LB's center of mass (CM) while EW is applied. The corresponding CAs are reported in Fig. 4. If a low voltage is applied or if the initial CA is already very low, the modified contact angle causes a marginal change on the meniscus of the LB, and hence the LB will not break [Mode 1 in Fig. 3(a)]. However, if the applied voltage is enough, then the CA significantly changes and finally the LB breaks. This happens in Figs. 3(b) (Mode 2) and 3(c) (Mode 3). In Fig. 3(b) the volume of the liquid and/or the initial CA on each surface hinders the LB reformation after the disruption. These two parameters of the system provide a favorable situation in Fig. 3(c) for LB reformation after the disruption. Therefore, in Fig. 3(c) the LB continues to break and reform with a certain period. Supplemental Material Movie 1 [59] shows the time history of the LB for Mode

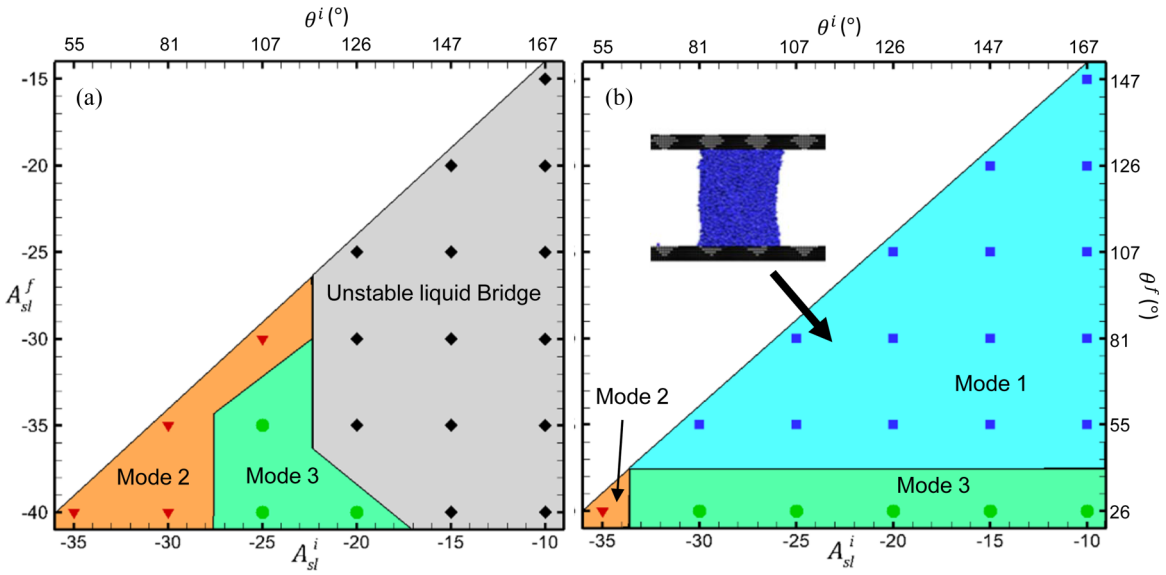

FIG. 5. Mode maps for three different cases. (a) Case 1 and (b) Cases 2 and 3. Blue squares indicate Mode 1; Red deltas indicate Mode 2; Green circles indicate Mode 3; Black diamonds indicate unstable liquid bridge.

3 [Fig. 3(c)]. While the previous three modes have been analyzed after getting a stable LB for $A^i_{s\ell}$ on each surface, it is also possible that by applying a specific $A^i_{s\ell}$ on the surfaces, the LB would not be stable between two surfaces. This is mainly due to the small volume of liquid and mainly happens for Case 1, which has 5508 liquid beads. The CM evolution of a sample case for this scenario is illustrated in Fig. 3(d), but it is not considered as one of the LB modes since it is not a stable LB. Figure 4 serves as a companion to Fig. 3 and provides information regarding local dynamic CA of the LB with respect to the lower horizontal wall versus time. Note that the errorbars in Fig. 4 give the standard deviation for the contact angle at 100 time steps around mean time, and this change is due to the random force. As can be seen from Figs. 4(b) and 4(c), before LB breaking, the contact angle reaches its minimum value. The break dramatically reduces the electric field on the solid-liquid interface, i.e., $B_r = 1$ and $A_{s\ell}$ returns to $A_{s\ell} = A^i_{s\ell}$. Hence, the CA suddenly increases, and the upper and lower liquids recoil. If the separated liquid parts on upper and lower walls later connect to each other, which happens in Fig. 4(c), the bridge forms again, CA decreases, and the cycle continues.

The mode map of each case is provided in Fig. 5. The unstable LBs for Case 1 have been shown with dark diamonds in Fig. 5(a). It is worth mentioning that, although Mode 3 can be observed in Case 1 with $A^i_{s\ell} = -25$ ($\theta^i = 107°$) and $A^f_{s\ell} = -35$ or -40 ($\theta^f = 55°$ or $26°$), due to the fewer number of particles compared with Cases 2 and 3, and lower energy compared with more hydrophobic initial conditions (e.g., $A^i_{s\ell} = -20$ ($\theta^f = 126°$) in Case 1), the two separated parts of the LB on each surfaces cannot meet each other as periodically as in other cases. Accordingly, these cases have not been included in the analyses for height at break, H', and transfer ratio, R, shown later. The behaviors of Cases 2 and 3 are very similar to each other. Hence, one map is provided for both cases [Fig. 5(b)]. In Fig. 5(b), most of the continuous break and reformation cases (Mode 3) happen when the EW provides a final $A^f_{s\ell} = -40$ ($\theta^f = 26°$).

The period for bridge breaking and reformation in Mode 3 shows a strong correlation to bridge height. To generalize the present results, different LB heights or plate spacings ($H_{\rm LB}$ from 10 to 20 DPD length) are considered, but the ratio of the cube of bridge height to volume is kept constant at $H^3_{\rm LB}/V = 0.253$. The initial and final contact angles in the test case in Figs. 3(c) and 4(c) are considered here. The droplet dynamics for these conditions are always in Mode 3. The intact bridge period τ_c, broken period τ_b, and the total duration of each cycle τ_t are reported. They monotonically increase with H^3 as shown in Fig. 6. This correlation suggests the ability to expand the results to other scales for similar operating conditions, e.g., operation contact angles.

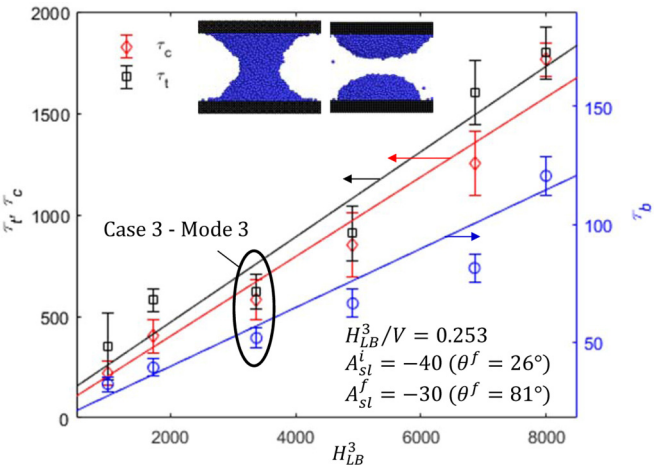

FIG. 6. Period of complete bridge, τ_c, bridge break, τ_b, and one cycle, τ_t, for Mode 3 using different liquid bridge height, $H_{\rm LB}$. For all cases, $H^3_{\rm LB}/N = 0.253$ and $A^i_{s\ell} = -30$ ($\theta^i = 81°$), $A^f_{s\ell} = -40$ ($\theta^f = 26°$), as shown in mode's map.

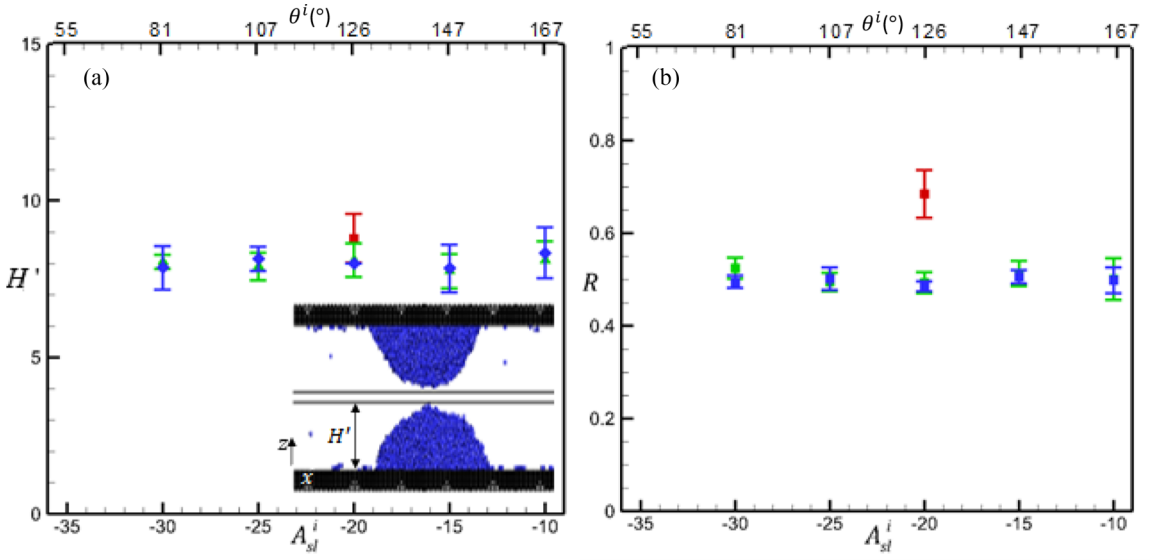

FIG. 7. Break height, H' (a), and mass ratio, R (b), for Mode 3 using different cases and $A^i_{s\ell}(\theta^i)$. Red square, green triangle, and blue diamond are for Cases 1 to 3, respectively. For all cases, $A^f_{s\ell} = -40(\theta^f = 26°)$ as shown in mode map.

The process of bridge breaking can also be characterized by the how the liquid is distributed following bridge breaking. We describe this distribution by the break height H' and transfer ratio R. The break height, H', is defined as the distance from the bottom plate where the bridge initially breaks, and the transfer ratio R is defined as the ratio of liquid transferred to the lower surface after bridge breaking over the total initial volume of the LB. Figure 7 provides break height H' and transfer ratio R versus $A^i_{s\ell}$ (and the corresponding initial CA) for LBs showing Mode 3 dynamics. Because of the symmetric nature of the EWOD system for these cases, the break height is almost always at the middle of the two surfaces and the transfer ratio is around 0.5. However, due to the low volume of the liquid in Case 1, randomness has a substantial effect on the LB, and hence, the break height, and transfer ratio show some asymmetry.

To provide a visual illustration regarding the somewhat random behavior of Case1, a case study with $A^i_{s\ell} = -25$ ($\theta^i = 107°$)) and $A^f_{s\ell} = -40$ ($\theta^f = 26°$) is considered in Fig. 8, which shows the center of mass versus time. As seen in this figure, the LB rupture and reformation is not as periodic as previous examples provided in Fig. 3. This is likely due to the lower volumes of separated liquids on each surface and the lower potential energy provided in this case [$A^i_{s\ell} = -25$ ($\theta^i = 107°$)] compared with the case having $A^i_{s\ell} = -20$ ($\theta^i = 126°$), both of which increase the influence of the random fluctuations in force.

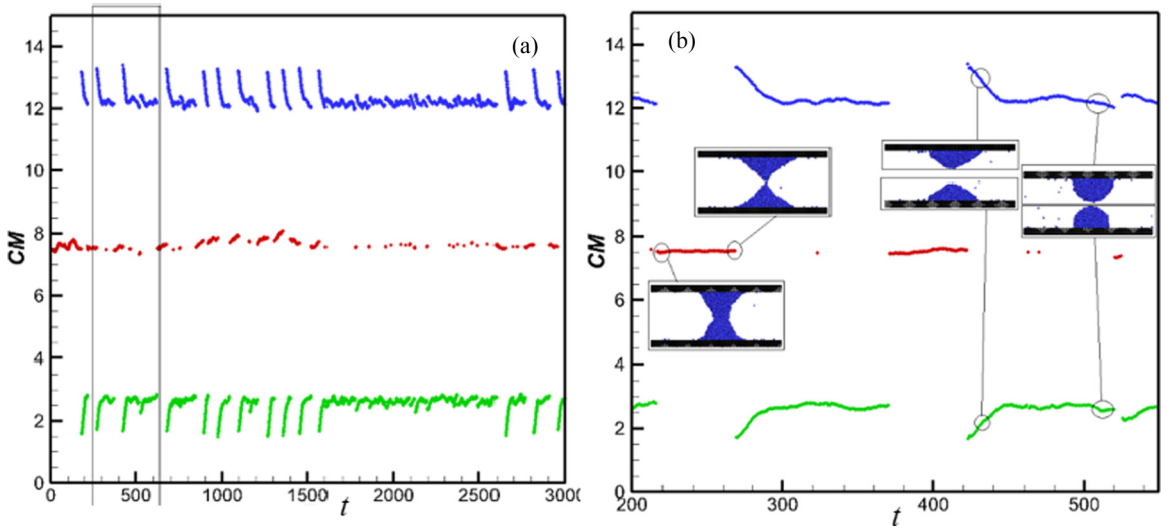

FIG. 8. Center of mass (CM) for Case 1 using $A^i_{s\ell} = -25(\theta^i = 107°)$ and $A^f_{s\ell} = -40$ ($\theta^f = 26°$). (a) The different behavior of the liquid bridge at different times due to the effect of randomness originating from the smaller number of liquid beads compared with other cases. (b) A detailed illustration of the cycles.

TABLE IV. Wettability parameters for upper and lower surfaces used for asymmetric investigations.

Case Number	lower wall $A^i_{s\ell}/\theta^i$	upper wall $A^i_{s\ell}/\theta^i$	lower wall $A^f_{s\ell}/\theta^f$	upper wall $A^f_{s\ell}/\theta^f$
Subcase 1			$-15/147^\circ$	$-20/126^\circ$
Subcase 2			$-20/126^\circ$	$-25/107^\circ$
Subcase 3	$-10/167^\circ$	$-15/147^\circ$	$-25/107^\circ$	$-30/81^\circ$
Subcase 4			$-30/81^\circ$	$-35/55^\circ$
Subcase 5			$-35/55^\circ$	$-40/26^\circ$

C. Asymmetric LB

If the material properties of the upper and lower surfaces are different, then the surface wettability and consequently the initial and final CAs of the liquid on upper and lower surfaces of the LB-EWOD system are also different. Hence, an asymmetric LB is formed between the two surfaces and it breaks in an asymmetric fashion. This phenomenon has been schematically shown in Fig. 1(b). The parameter space of the asymmetric LB is much larger due to the additional degree of freedom in surface wettability. Hence, the current investigation of asymmetric LB-EWOD has been limited to five subcases provided in Table IV.

Similar to symmetric cases, these asymmetric cases may break the bridge permanently, or may continuously break and reform the LB. Samples of CM time histories are given in Figs. 9(a) and 9(c) for two case studies. The detailed illustration of one cycle for each case has been provided in Figs. 9(b) and 9(d). In these two examples, a lower CA has been assigned to the upper wall and a higher CA has been assigned to the lower wall. It can be seen from the inset figures, in both cases, that, since the upper wall is more hydrophilic compared with the lower wall, the upper wall holds more liquid and the bridge breaks in a completely asymmetric configuration. As can be seen in both figures, the small amount of liquid on the lower wall may separate from the surface and form a satellite droplet. This can be clearly seen in the inset in Fig. 9(b). When the LB breaks, the electric field on the solid-liquid interface decreases and the initial CA is restored on each surface, and therefore the liquid recoils from the upper surface and again may form a bridge between the two surfaces. Supplemental Material Movie 2 [59] shows

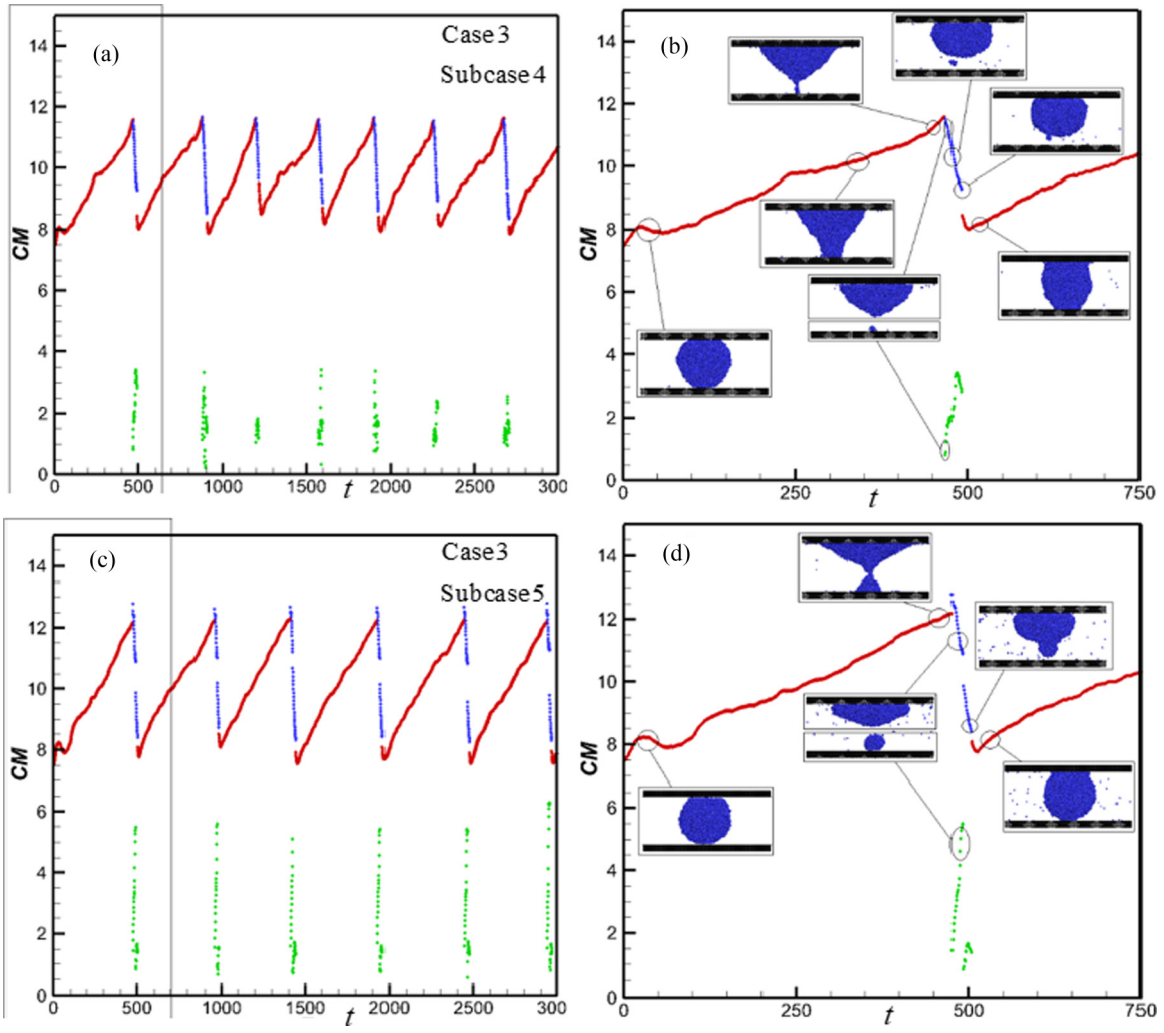

FIG. 9. Center of mass (CM) for two different asymmetric case studies (a, c), and an illustration of one cycle for each case (b, d).

TABLE V. Different modes of bridge behavior for studied asymmetric cases.

Case number/Subcase Number	Subcase 1	Subcase 2	Subcase 3	Subcase 4	Subcase 5
Case 1	–	–	–	–	–
Case 2	Mode 3	Mode 3	Mode 3	Mode 3	Mode 3
Case 3	Mode 1	Mode 1	Mode 3	Mode 3	Mode 3

the time history of a LB while it breaks and reforms for the case given in Fig. 9(a). If the volume of the liquid or the initial CA of the liquid on the surface is not favorable for bridge formation, the liquid may attach to the upper surface and may not form an LB. For geometric and material parameters used, this happens for all subcases of Case 1, which only has 5,508 beads. Similar to Fig. 3(d), in these scenarios the initial LB is not stable, and hence this is not included within the available modes. The cases and their associated dynamic mode have been summarized in Table V.

In Fig. 10, the effect of LB height, H_{LB}, on the period of the oscillatory system dynamics is reported for the asymmetric system, with $H_{\mathrm{LB}}^3/V = 0.253$ for subcase 4 of case 3. The figure shows the periods τ_c, τ_t, and τ_c versus H_{LB}^3. Mode 3 was observed for all the simulations considered in this figure, and the periods are linearly increasing with H_{LB}^3. The periods are smaller and have larger variability compared with the symmetric data presented in Fig. 6. The values of break height and transfer ratio for the asymmetric systems are given in Fig. 11. Because of the asymmetric nature, the break height H' is generally small and often approximately zero, $H' \approx 0$. Likewise, $R \approx 0$ for almost all case studies as shown in Fig. 11(b). In some cases in Fig. 11(a), H' is not equal to zero, but the amount of liquid between the lower surface and the breakpoint is marginal and does not substantially affect the value of R. This phenomenon is illustrated in the insets of Figs. 9(b) and 9(d).

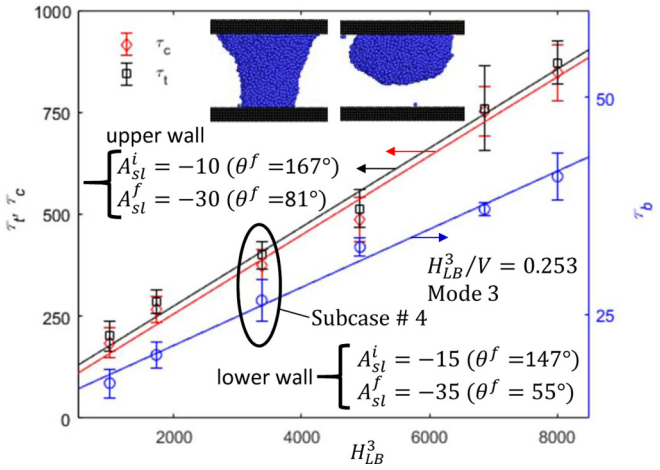

FIG. 10. Period of complete bridge, τ_c, bridge break, τ_b, and one cycle, τ_t, for subcase 4 with different height, H_{LB}, and $H_{\mathrm{LB}}^3/N = 0.253$.

V. CONCLUSION

A microscale liquid oscillator is proposed using EWOD. MDPD simulations have been conducted for both symmetric and asymmetric LBs with EWOD. By changing the wettability characteristics of the upper and lower surfaces, the LB's meniscus deforms. It was shown that depending on the modified wettability of the surfaces, the LB may or may not break. Three different dynamic modes for evolution of both symmetric and asymmetric LBs with respect to EWOD have been realized. Increasing the initial value of CA, i.e., increasing $A_{s\ell}^i$, increases the duration of time for which the bridge is complete and decreases the duration for which it is broken. The total time duration for one cycle is also changed for different values of $A_{s\ell}^i$. It was shown that LBs between plates with similar wettability usually rupture symmetrically, while for asymmetric LBs rupture mainly happens nearer the surface with lower wettability. Similar behavior is seen in the ratio

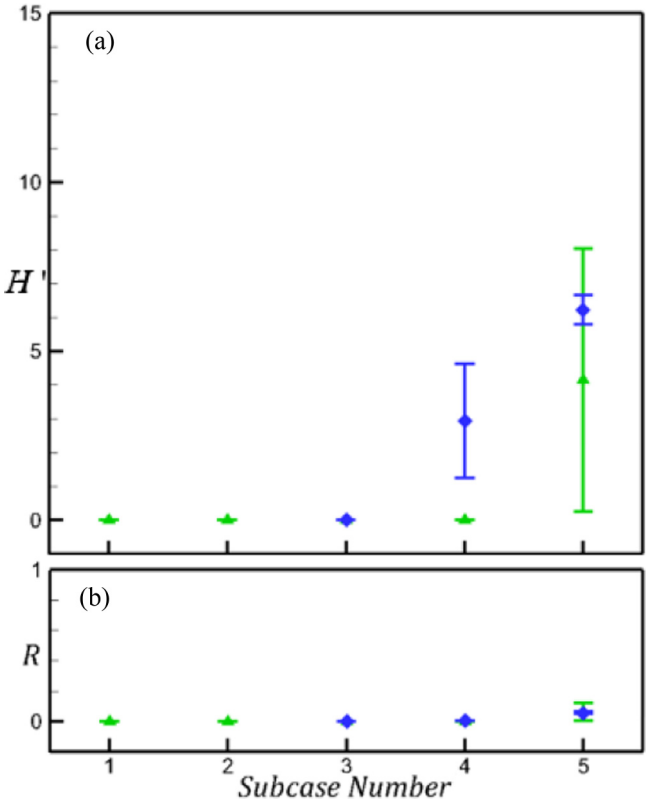

FIG. 11. Break height (a) and mass ratio (b) for Mode 3 in Cases 2 and 3 with wettability given in Table V. Green triangles and blue diamonds are for cases 2 and 3, respectively.

of liquid left on each surface after rupture. Satellite droplets have been observed in asymmetric cases. These droplets form from a small amount of liquid on the surface with low wettability, which jumps away from the surface when the wettability of the surface returns to its original value after the LB breaks. The data provided in this investigation can help to understand the fundamental physics behind the effects of EW between parallel surfaces. The results also provide design guidance for a microscale liquid oscillator using EWOD.

ACKNOWLEDGMENT

The support for our research by the National Science Foundation (Grant No. 1718194) is greatly appreciated.

[1] D. Yuan, Fundamentals and applications of inertial microfluidics: A review, Lab Chip. **16**, 10 (2016).
[2] K. Choi, A. H. C. Ng, R. Fobel, and A. R. Wheeler, Digital microfluidics, Annu. Rev. Anal. Chem. **5**, 413 (2012).
[3] E. Samiei, M. Tabrizian, and M. Hoorfar, A review of digital microfluidics as portable platforms for lab-on a-chip applications, Lab Chip. **16**, 2376 (2016).
[4] Y. Li, C. Diddens, A. Prosperetti, K.L. Chong, X. Zhang, and D. Lohse, Bouncing Oil Droplet in a Stratified Liquid and Its Sudden Death, Phys. Rev. Lett. **122**, 154502 (2019).
[5] D. Quéré, Wetting and roughness, Annu. Rev. Mater. Res. **38**, 71 (2008).
[6] W. D. Kaplan, D. Chatain, P. Wynblatt, and W. C. Carter, A review of wetting versus adsorption, complexions, and related phenomena: The rosetta stone of wetting, J. Mater. Sci. **48**, 5681 (2013).
[7] P. Purswani, M. S. Tawfik, and Z. T. Karpyn, Factors and mechanisms governing wettability alteration by chemically tuned waterflooding: A review, Energy Fuels **31**, 7734 (2017).
[8] M. E. Foulaadvand and N. Ojaghlou, Structural and elastic properties of a confined two-dimensional colloidal solid: A molecular dynamics study, Phys. Rev. E **86**, 021405 (2012).
[9] N. Ojaghlou, H. V. Tafreshi, D. Bratko, and A. Luzar, Dynamical insights into the mechanism of a droplet detachment from a fiber, Soft Matter **14**, 8924 (2018).
[10] M. Abolghasemibizaki, C. J. Robertson, C. P. Fergusson, R. L. McMasters, and R. Mohammadi, Rolling viscous drops on a non-wettable surface containing both micro- and macro-scale roughness, Phys. Fluids **30**, 023105 (2018).
[11] F. Mugele and J.-C. Baret, Electrowetting: From basics to applications, J. Phys.: Condens. Matter **17**, R705 (2005).
[12] L. Chen and E. Bonaccurso, Electrowetting: From statics to dynamics, Adv. Colloid Interface Sci. **210**, 2 (2014).
[13] M. Abdelgawad and A. R. Wheeler, The Digital Revolution: A New Paradigm for Microfluidic, Adv. Mater. **21**, 920 (2009).
[14] M. W. J. Prins, W. J. J. Welters, and J. W. Weekamp, Fluid control in multichannel structures by electrocapillary pressure, Science **291**, 277 (2001).
[15] A. A. Hemeda and H. V. Tafreshi, General Formulations for Predicting Longevity of Submerged Superhydrophobic Surfaces Composed of Pores or Posts, Langmuir **30**, 10317 (2014).
[16] B. Berge, Électrocapillarité et mouillage de films isolants par l'eau, Comptes Rendus l'Académie Des Sci. Série II. **317**, 157 (1992).
[17] D. Jiang and S. Y. Park, Light-driven 3D droplet manipulation on flexible optoelectrowetting devices fabricated by a simple spin-coating method, Lab Chip. **16**, 1831 (2016).
[18] G. McHale, C. V. Brown, M. I. Newton, G. G. Wells, and N. Sampara, Dielectrowetting Driven Spreading of Droplets, Phys. Rev. Lett. **107**, 186101 (2011).
[19] F. Xia, Y. Zhu, L. Feng, and L. Jiang, Smart responsive surfaces switching reversibly between super-hydrophobicity and superhydrophilicity, Soft Matter. **5**, 275 (2009).
[20] S. J. Lee, J. Hong, K. H. Kang, I. S. Kang, and S. J. Lee, Electrowetting-induced droplet detachment from hydrophobic surfaces, Langmuir **30**, 1805 (2014).
[21] K. Ashoke Raman, R. K. Jaiman, T. S. Lee, and H. T. Low, A numerical study on electrowetting-induced jumping and transport of droplet, Int. J. Heat Mass Transf. **99**, 805 (2016).
[22] A. Cavalli, D. J. Preston, E. Tio, D. W. Martin, N. Miljkovic, E. N. Wang, F. Blanchette, and J. W. M. Bush, Electrically induced drop detachment and ejection, Phys. Fluids **28**, 022101 (2016).
[23] J. Hong, Y. K. Kim, K. H. Kang, J. Kim, and S. J. Lee, Spreading dynamics and oil film entrapment of sessile drops submerged in oil driven by DC electrowetting, Sens. Actuators B: Chem. **196**, 292 (2014).
[24] W. C. Nelson, P. Sen, and C. J. C. J. Kim, Dynamic contact angles and hysteresis under electrowetting-on-dielectric, Langmuir **27**, 10319 (2011).
[25] E. Bormashenko, R. Pogreb, S. Balter, and D. Aurbach, Electrically controlled membranes exploiting cassie-wenzel wetting transitions, Sci. Rep. **3**, 3028 (2013).
[26] S. Wang, H. H. Chen, and C. L. Chen, Electrowetting-on-dielectric assisted bubble detachment in a liquid film, Appl. Phys. Lett. **108**, 181601 (2016).
[27] D. Baratian, A. Cavalli, D. Van Den Ende, and F. Mugele, On the shape of a droplet in a wedge: New insight from electrowetting, Soft Matter. **11**, 7717 (2015).
[28] N. Li, L. Wu, C. Yu, H. Dai, T. Wang, Z. Dong, and L. Jiang, Ballistic jumping drops on superhydrophobic surfaces via electrostatic manipulation, Adv. Mater. **30**, 1703838 (2018).
[29] S. Arscott, Electrowetting and semiconductors, RSC Adv. **4**, 29223 (2014).
[30] T. Krupenkin and J. A. Taylor, Reverse electrowetting as a new approach to high-power energy harvesting, Nat. Commun. **2**, 448 (2011).
[31] Y. Wang, H. Li, L. Zhao, B. Wu, S. Liu, Y. Liu, and J. Yang, A review of droplet resonators: Operation method and application, Opt. Laser Technol. **86**, 61 (2016).
[32] B. Berge and J. Peseux, Variable focal lens controlled by an external voltage: An application of electrowetting, Eur. Phys. J. E **3**, 159 (2000).
[33] S. K. Chung, K. Ryu, and S. K. Cho, Electrowetting propulsion of water-floating objects, Appl. Phys. Lett. **95**, 014107 (2009).

[34] S. Schuhladen, K. Banerjee, M. Stürmer, P. Müller, U. Wallrabe, and H. Zappe, Variable optofluidic slit aperture, Light: Sci. Appl. **5**, e16005 (2016).

[35] J. Hong, Y. K. Kim, D.-J. Won, J. Kim, and S. J. Lee, Three-dimensional digital microfluidic manipulation of droplets in oil medium, Sci. Rep. **5**, 10685 (2015).

[36] T.-H. Hsu, S. Manakasettharn, J. A. Taylor, and T. Krupenkin, Bubbler: A novel ultra-high power density energy harvesting method based on reverse electrowetting, Sci. Rep. **5**, 16537 (2015).

[37] B. Roman and J. Bico, Elasto-capillarity: Deforming an elastic structure with a liquid droplet, J. Phys.: Condens. Matter **22**, 493101 (2010).

[38] A. Klingner, S. Herminghaus, and F. Mugele, Self-excited oscillatory dynamics of capillary bridges in electric fields, Appl. Phys. Lett. **82**, 4187 (2003).

[39] P. Español and P. B. Warren, Perspective: Dissipative particle dynamics, J. Chem. Phys. **146**, 150901 (2017).

[40] A. Ghoufi, J. Emile, and P. Malfreyt, Recent advances in many body dissipative particles dynamics simulations of liquid-vapor interfaces, Eur. Phys. J. E **36**, 10 (2013).

[41] A. Boromand, S. Jamali, and J. M. Maia, Viscosity measurement techniques in dissipative particle dynamics, Comput. Phys. Commun. **196**, 149 (2015).

[42] A. Ghoufi and P. Malfreyt, Mesoscale modeling of the water liquid-vapor interface: A surface tension calculation, Phys. Rev. E **83**, 051601 (2011).

[43] E. Abu-Nada, Dissipative particle dynamics simulation of combined convection in a vertical lid driven cavity with a corner heater, Int. J. Therm. Sci. **92**, 72 (2015).

[44] L. Lei, E. Louis, B. Cheong, and N. Phan-thien, Many-body dissipative particle dynamics (MDPD) simulation of a pseudoplastic yield-stress fluid with surface tension in some flow processes, J. Non-Newton. Fluid Mech. **260**, 163 (2018).

[45] A. Mishra, A. Hemeda, M. Torabi, J. Palko, S. Goyal, D. Li, and Y. Ma, A simple analytical model of complex wall in multibody dissipative particle dynamics, J. Comput. Phys. **396**, 416 (2019).

[46] P. B. Warren, Vapor-liquid coexistence in many-body dissipative particle dynamics, Phys. Rev. E **68**, 066702 (2003).

[47] M. Ahmadlouydarab, C. Lan, A. K. Das, and Y. Ma, Coalescence of sessile microdroplets subject to a wettability gradient on a solid surface, Phys. Rev. E **94**, 033112 (2016).

[48] K. C. Ng and T. W. H. Sheu, Refined energy-conserving dissipative particle dynamics model with temperature-dependent properties and its application in solidification problem, Phys. Rev. E **96**, 043302 (2017).

[49] M. Arienti, W. Pan, X. Li, and G. Karniadakis, Many-body dissipative particle dynamics simulation of liquid/vapor and liquid/solid interactions, J. Chem. Phys. **134**, 204114 (2011).

[50] Z. Li, X. Bian, Y. Tang, and G. Em, A dissipative particle dynamics method for arbitrarily complex geometries, J. Comput. Phys. **355**, 534 (2018).

[51] M. P. Allen and D. J. Tildesley, *Computer Simulation of Liquids, Second Edition* (Oxford University Press, Oxford, 2017).

[52] K. Zhang, Z. Li, M. Maxey, S. Chen, and G. E. Karniadakis, Self-cleaning of hydrophobic rough surfaces by coalescence-induced wetting transition, Lamgmuir **35**, 2431 (2019).

[53] B.-Y. Cao, M. Chen, and Z.-Y. Guo, Liquid flow in surface-nanostructured channels studied by molecular dynamics simulation, Phys. Rev. E **74**, 066311 (2006).

[54] G. S. Jung, J. S. Lee, and Y. H. Won, Effects of liquid property and substrate roughness on the response time of an electrowetting liquid lens, Proc. SPIE **10545**, 1054516 (2018).

[55] M. Torabinia, A. Farzbod, and H. Moon, Electromechanical model to predict the movability of liquids in an electrowetting-on-dielectric microfluidic device, J. Appl. Phys. **123**, 154902 (2018).

[56] C. C. Chang, Y. J. Sheng, and H. K. Tsao, Wetting hysteresis of nanodrops on nanorough surfaces, Phys. Rev. E **94**, 042807 (2016).

[57] A. A. Hemeda, R. J. A. Esteves, J. T. McLeskey, M. Gad-el-Hak, M. Khraisheh, and H. Vahedi Tafreshi, Molecular dynamic simulations of fibrous distillation membranes, Int. Commun. Heat Mass Transf. **98**, 304 (2018).

[58] P. B. Paramonov and S. F. Lyuksyutov, Density-functional description of water condensation in proximity of nanoscale asperity, J. Chem. Phys. **123**, 084705 (2005).

[59] See Supplemental Material at http://link.aps.org/supplemental/10.1103/PhysRevE.100.033102 for supplementary movies 1 and 2.